



Article

Photoelectrochemical Water Splitting and H₂ Generation Enhancement Using an Effective Surface Modification of W-Doped TiO₂ Nanotubes (WT) with Co-Deposition of Transition Metal Ions

Tecush Mohammadi ^{1,*} , Somayeh Sharifi ², Yousef Ghayeb ¹, Tayebeh Sharifi ^{1,3,*} 
and Mohamad Mohsen Momeni ¹

¹ Department of Chemistry, Isfahan University of Technology, Isfahan 84156-83111, Iran

² Department of Chemistry, Bu-Ali Sina University, Hamedan 65167-38695, Iran

³ Ruđer Bošković Institute, Bijenička Cesta 54, 10000 Zagreb, Croatia

* Correspondence: t.mohammadi@alumni.iut.ac.ir (T.M.); tsharifi@irb.hr (T.S.)

Abstract: W-doped TiO₂ nanotube arrays (WT) were fabricated by in situ electrochemical anodization of titanium substrate. The results of the influence of different photo-deposited transition ions (Cr_xFe_{1-x}, 0 ≤ x ≤ 1) on the surface of WT on photoelectrochemical (PEC) water splitting and H₂ generation are presented. The crystallinities, structural, elemental, and absorption analysis were conducted by XRD, SEM, RAMAN, EDX, and UV-Vis absorption spectroscopy, which demonstrated anatase as the main crystalline phase of TiO₂, and the existence of Cr_xFe_{1-x} (nano)particles/film deposited on the surface of WT. The SEM images revealed that the deposition rate and morphology are highly related to the ratio of Cr and Fe ions. Under visible light illumination, the entire photoelectrodes showed a very good response to light with stable photocurrent density. PEC measurements revealed that the mixture of transition ions with a certain ratio of ions (Cr_{0.8}Fe_{0.2}-T) led to enhanced photocurrent density more than that of other modifiers due to decreasing charge recombination as well as improving the charge transfer. Moreover, PEC water splitting was conducted in an alkaline solution and the Cr_{0.8}Fe_{0.2}-T photoelectrode generated 0.85 mL cm⁻² h⁻¹ H₂, which is over two times that of pristine WT.

Keywords: TiO₂ nanotubes; in situ electrochemical anodization; transition metals; hydrogen; water splitting



Citation: Mohammadi, T.; Sharifi, S.; Ghayeb, Y.; Sharifi, T.; Momeni, M.M. Photoelectrochemical Water Splitting and H₂ Generation Enhancement Using an Effective Surface Modification of W-Doped TiO₂ Nanotubes (WT) with Co-Deposition of Transition Metal Ions.

Sustainability **2022**, *14*, 13251.
<https://doi.org/10.3390/su142013251>

Academic Editor: Kaan Kalkan

Received: 12 September 2022

Accepted: 12 October 2022

Published: 14 October 2022

Publisher's Note: MDPI stays neutral with regard to jurisdictional claims in published maps and institutional affiliations.



Copyright: © 2022 by the authors. Licensee MDPI, Basel, Switzerland. This article is an open access article distributed under the terms and conditions of the Creative Commons Attribution (CC BY) license (<https://creativecommons.org/licenses/by/4.0/>).

1. Introduction

Hydrogen (H₂) as renewable energy has attracted significant attention to be the best replacement for fossil fuels to move toward a decarbonized future owing to unique properties such as high efficiency and energy density (120–142 MJ/kg), the ability to obtain from H₂O and generate only H₂O with its combustion [1,2]. Photoelectrochemical (PEC) water splitting using sunlight is the most promising strategy to generate hydrogen. Early work on TiO₂ for water splitting and PEC H₂ generation was reported by Fujishima and Honda in 1972 [3]. Since then, extensive efforts have been invested in exploring and introducing new materials such as WO₃, MnO_x, Bismuth-based nanomaterials, and Fe₂O₃ [4–7]. Although a large number of semiconductors have been inspected over the past few decades, TiO₂ is still particularly appealing because of suitable band-edge positions and relatively good stability in different electrolytes as well as photo-corrosion resistance [8,9]. The TiO₂ nanotube (NTs) structures, as one-dimensional (1D) nanostructures, have been considered highly promising candidates with high efficiency in PEC water splitting because of high specific surface area, electron mobility, and mechanical strength [10,11]. However, pristine TiO₂ is still suffering from the utilization of less than 5% of sunlight, thanks to its wide band gap (≥3.0 eV) [12] and its modification is necessary to improve photo-response in the visible

range and enhance the efficiency of chemical solar energy conversion [13,14]. To achieve this, many efforts have been made such as composites with other metal oxide and/or carbon-based materials, metal or non-metal doping, and surface modification [13,15–17]. For example, composite with other semiconductors such as WO_3 applied in this work, not only enhances the visible light absorption but also increases the photo-generated charge (e^-/h^+) separation [18]. Another simple and effective technique is through the TiO_2 NTs surface modification, especially with the transition metals. Transition metals can improve PEC activities of TiO_2 NTs through (i) decreasing the band gap by introducing new sub-levels because of partially filled D-orbitals, and (ii) decreasing charge recombination by trapping photo-generated charge (e^-/h^+) of TiO_2 [9,19,20]. Suligoj et al. have recently reported that deposited transition metal ion clusters on the TiO_2 , via surface modification, can also act as co-catalysts and improve the photocatalytic activity of TiO_2 [21].

There are several methods to deposit transition metal (oxide) particles on the surface of TiO_2 NTs such as sputtering, chemical bath deposition, electrodeposition, and photo-deposition [13,21–25]. Among these, photo-deposition is one of the easiest methods that does not need an elevated temperature or applied (bias) potential. Moreover, adjusting some parameters in this method (metal precursor, pH, sacrificial reagent, time of deposition, etc.), gives the possibility to control the size and geometrical distribution, and oxidation state of the deposited (nano)particles [15,22,26].

In this work, self-organized WO_3 doped TiO_2 NTs (WT) were successfully fabricated through an optimized in situ electrochemical anodization of titanium substrate according to our previous studies [13]. Then, Fe and Cr ions were chosen for the WT surface modification via the photo-deposition method. Different mixtures of them, $\text{Cr}_x\text{Fe}_{1-x}$ ($0 \leq x \leq 1$), were also prepared for photo-deposition to clarify the effects of different ratios of two transition metal ions. The $\text{Cr}_x\text{Fe}_{1-x}\text{-T}$ ($0 \leq x \leq 1$) abbreviation has been used throughout the manuscript; x stands for the molar ratio of Cr and Fe ions used in the photo-deposition precursor for the WT surface modification. $\text{Cr}_x\text{Fe}_{1-x}\text{-T}$ ($0 \leq x \leq 1$) photoelectrodes were submitted for thorough material characterization, electrochemical and semiconducting properties, and the activity in PEC water splitting for H_2 evolution.

2. Materials and Methods

2.1. Materials

Titanium foils (Ti, 99%) with 1 mm thickness, sodium tungstate dihydrate ($\text{Na}_2\text{WO}_4 \times 2 \text{H}_2\text{O}$, 99%), hydrogen fluoride (HF, 40%), nitric acid (HNO_3 , 65%), dimethyl sulfoxide ($\text{C}_2\text{H}_6\text{SO}$, 99.5%), ethanol ($\text{C}_2\text{H}_6\text{O}$, 99%), potassium hydroxide (KOH, 499%), ethylene glycol ($\text{C}_2\text{H}_6\text{O}_2$, 99.5%), potassium chromate (K_2CrO_4 , 99.5%), and iron (III) chloride hexahydrate ($\text{FeCl}_3 \times 6 \text{H}_2\text{O}$, 99%) were purchased from commercial sources and were used as purchased and without further purification. Solutions were prepared using deionized (DI) water within this work.

2.2. In Situ Electrochemical Anodization Procedure

The TiO_2 NTs were prepared by in situ electrochemical anodization with the two-electrode system including Ti foil and platinum-coated titanium mesh electrodes as anode and cathode electrodes, respectively. Prior to anodization, the surface of Ti sheets ($1 \times 3 \text{ cm}^2$) was polished with different emery types of abrasive papers and then cleaned by rinsing with DI water. Afterward, Ti sheets were chemically etched with a mixture of HF: HNO_3 : H_2O in a volume ratio of 1:4:5 for 30 s at room temperature and then washed with DI water. In situ electrochemical anodization was performed at 40 V for 8 h in a solution of dimethyl sulfoxide as an electrolyte containing 12 mM of sodium tungstate dihydrate, HF (2 vol%), and H_2O (1 vol%). Finally, as-anodized amorphous W-doped TiO_2 nanotubes were annealed at 400 °C in air for 2 h, with a heating rate of 2 °C min^{-1} (F3L-1720, AZAR Furnaces, Tehran, Iran) (Figure 1A).

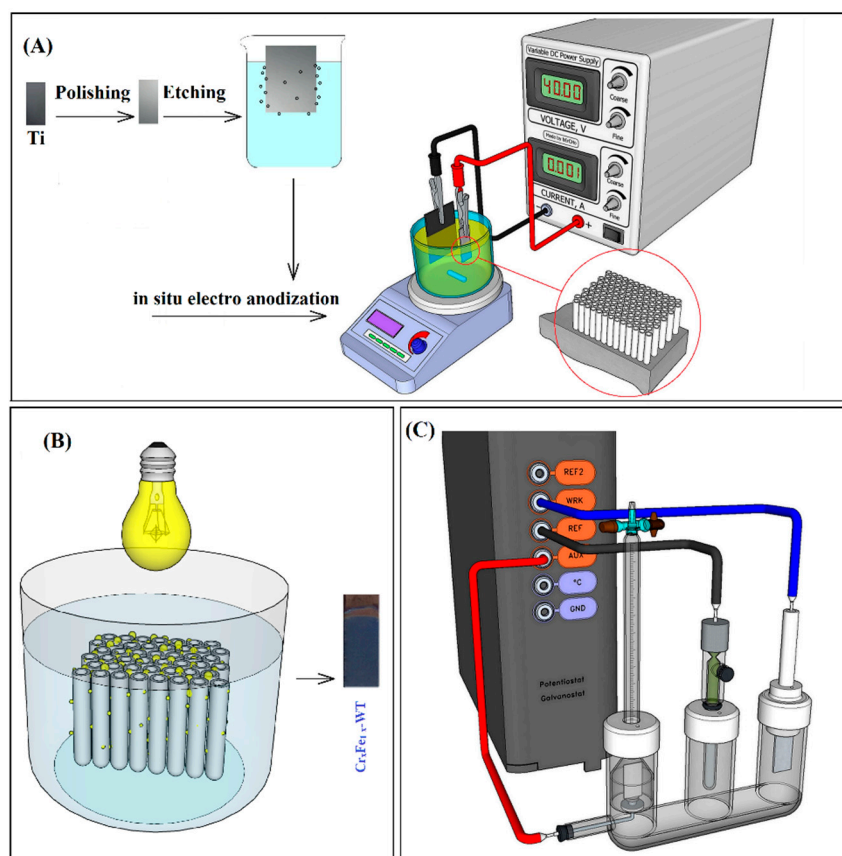


Figure 1. Schematic presentation of fabrication of WT nanotubes by in situ electrochemical anodization (A) $\text{Cr}_x\text{Fe}_{1-x}\text{-T}$ by photo-deposition (B) and measuring H_2 evolution from PEC water splitting using an inverted burette (C).

2.3. Photo-Deposition Procedure

Surface modification of WT with $\text{Cr}_x\text{Fe}_{1-x}$ ($0 \leq x \leq 1$) was accomplished using the photo-deposition method. Briefly, the WT electrodes were soaked in 25 mL precursor of K_2CrO_4 (10 mM), or $\text{FeCl}_3 \times 6\text{H}_2\text{O}$ (10 mM), and different molar ratio of Fe and Cr as $\text{Cr}_x\text{Fe}_{1-x}$, ($x = 0, 0.2, 0.4, 0.5, 0.6, 0.8$, and 1), containing ethanol (10 vol%). Photo-deposition was performed by illuminating the solution in which WT electrodes were immersed with a high-pressure mercury lamp (400 W) for 1 h. After the photo-deposition, photoelectrodes were washed with DI water (Figure 1B). Accordingly, obtained photoelectrodes are denoted onward throughout the manuscript as $\text{Cr}_x\text{Fe}_{1-x}\text{-T}$ ($x = 0, 0.2, 0.4, 0.5, 0.6, 0.8$, and 1), corresponding to the used molar ratio of Fe and Cr in the photo-deposition precursor.

2.4. Material Characterization

A Philips XL30 (Eindhoven, The Netherlands) field-emission scanning electron microscope equipped with an energy dispersive X-ray (EDX) mapping port was used to characterize the morphology and the elemental distribution of the microscopic region of the materials. X-ray diffraction using a PMD Philips X-Pert (Panalytical, Almelo, The Netherlands) was used for crystal structure characterization. The Raman spectra of the samples were obtained with a TakRam N1-541 (Tehran, Iran) Raman spectrometer. Moreover, the UV-vis absorption spectra were measured by a JASCO V-570 (Tokyo, Japan) UV-vis spectrophotometer.

2.5. Photoelectrochemical (PEC) Characterization and PEC Water Splitting

PEC measurements were carried out in KOH (1 M, pH = 13.9) solution containing ethylene glycol (5 vol%) with a potentiostat/galvanostat OGF 500 (Origsflex, Lyon, France).

Linear sweep voltammetry (LSV), chronoamperometry (CA), and open circuit potential (OCP) measurements were conducted in a standard three-electrode configuration including as-prepared $\text{Cr}_x\text{Fe}_{1-x}\text{-WT}$ photoelectrodes, Ag/AgCl electrode, and platinum foil as working electrode, reference electrode, and counter electrode, respectively (Figure 1C). All of these electrochemical tests were carried out in the presence, absence, and chopped light. The photoelectrodes were illuminated by a 35 W Xenon (Xe) lamp (200 mW cm^{-2}) equipped with a UV cut-off filter ($\lambda < 420 \text{ nm}$). The potential of the photoelectrodes was reported versus (vs.) the reversible hydrogen electrode (RHE) using Equation (1):

$$E_{\text{RHE}} = 0.1976 \text{ V} + 0.059 \text{ pH} + E_{\text{Ag/AgCl}} \quad (1)$$

The electrochemical impedance spectra (EIS) were also performed on the electrochemical workstation system Zahner Zenium Pro (Zahner-Elektrik, Kronach, Germany) in a range of 100 kHz–100 mHz under 1.22 V vs. RHE and a DC voltage of 10 mV amplitude in the dark and under illumination in the same electrolyte used in PEC measurements.

The same three-electrode configuration was used for PEC water splitting (Figure 1C). $\text{Cr}_x\text{Fe}_{1-x}\text{-WT}$ photoelectrodes were placed in the anodic chamber while immersed in KOH (1 M, pH = 13.9) solution containing ethylene glycol (5 vol%) and irradiated by Xe lamp (200 mW cm^{-2} , and $\lambda > 420 \text{ nm}$). A platinum-coated titanium mesh electrode as the cathode was inserted into an inverted burette, where H_2 was collected [27–29]. PEC water splitting was continued by applying a constant external potential of 1.23 V vs. RHE. The volume of the produced hydrogen gas was quantitatively measured via electrolyte displacement level in the inverted burette at predefined time (Figure 1C).

3. Results and Discussion

3.1. Material Characterization

Our previous results revealed that highly ordered WT was fabricated through in situ electrochemical anodization of Ti foil in an electrolyte containing Na_2WO_4 . Although, the concentration of Na_2WO_4 did not show a significant influence on WT morphology. However, the PEC activity of fabricated WT can change and the maximum PEC activity for WT was obtained using $\sim 12 \text{ mM}$ of Na_2WO_4 as an optimum concentration [13,30]. Hence, in this work, WT photoelectrode was fabricated according to the optimal conditions established in our previous studies [13,30].

The surface morphology of pristine WT nanotubes can be seen in Figure 2. Uniform and highly ordered nanotubes were observed with an average inner diameter and wall thickness of about 110 nm and 25 nm, respectively. The surface modification of WTs was then performed with the photo-deposition of $\text{Cr}_x\text{Fe}_{1-x}$ ($0 \leq x \leq 1$) and their SEM images have been compared in Figure 3. In the case of $\text{Cr}_0\text{Fe}_1\text{-WT}$, the precursor of photo-deposition only consisted of Fe ions, particles with sizes of $\leq 200 \text{ nm} \times 200 \text{ nm}$ were observed on the WT surface (Figure 3A). Although particles are fairly homogeneously distributed over the WT surface, some of them covered the top of the nanotubes (Figure 3A) which might decrease PEC activity.

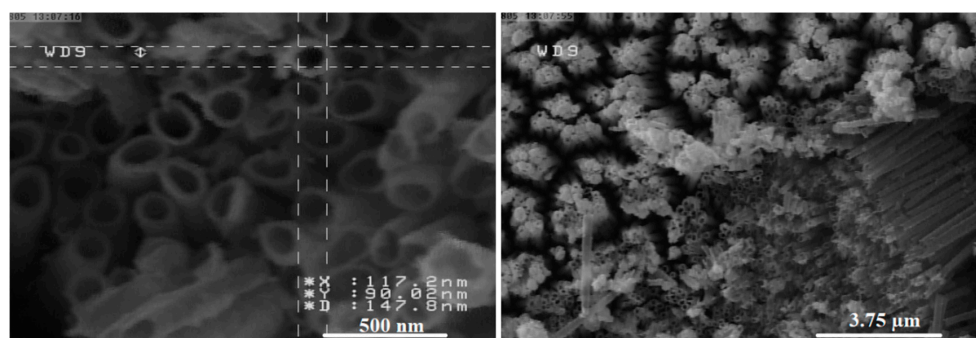


Figure 2. SEM images of WT photoelectrode.

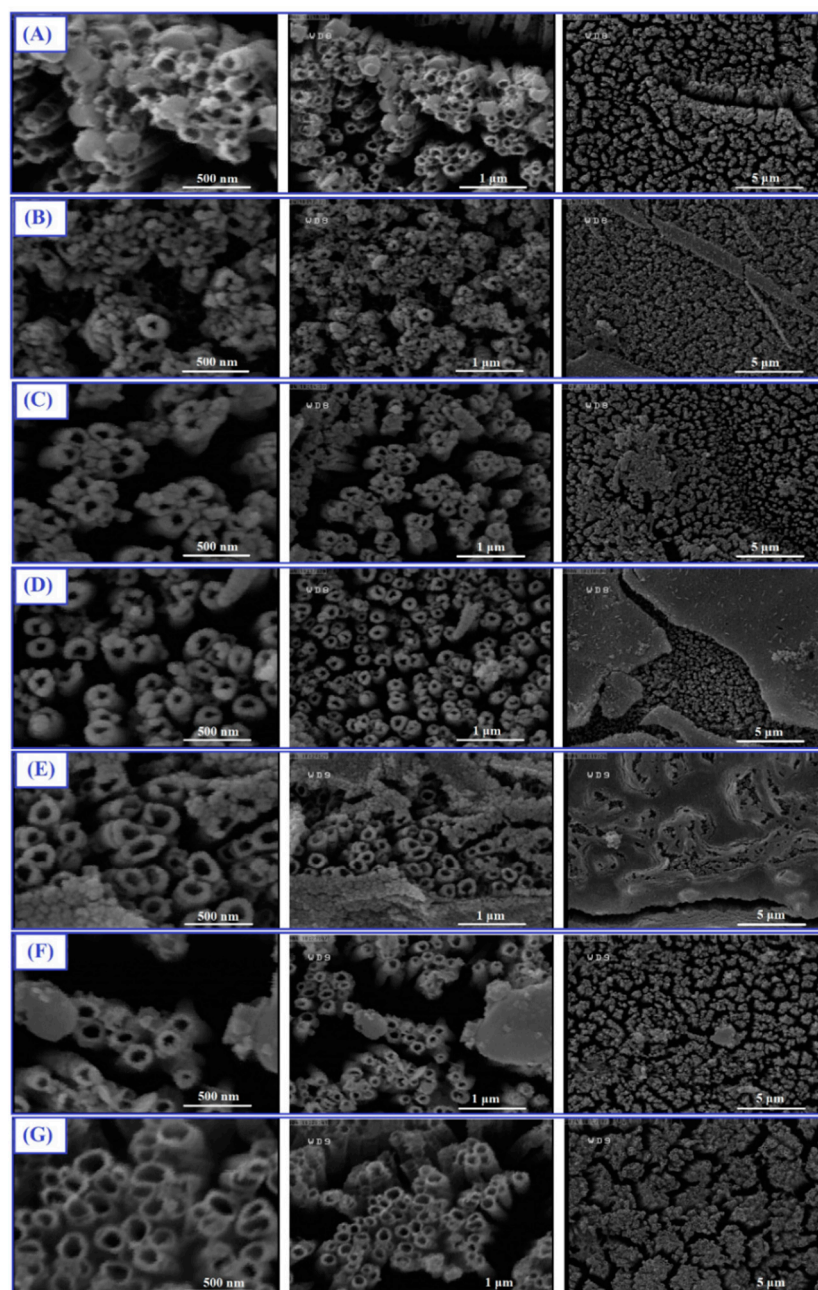


Figure 3. SEM images of $\text{Cr}_0\text{Fe}_1\text{-WT}$ (A), $\text{Cr}_{0.2}\text{Fe}_{0.8}\text{-WT}$ (B), $\text{Cr}_{0.4}\text{Fe}_{0.6}\text{-WT}$ (C), $\text{Cr}_{0.5}\text{Fe}_{0.5}\text{-WT}$ (D), $\text{Cr}_{0.6}\text{Fe}_{0.4}\text{-WT}$ (E), $\text{Cr}_{0.8}\text{Fe}_{0.2}\text{-WT}$ (F), $\text{Cr}_1\text{Fe}_0\text{-WT}$ (G) at different magnifications.

Interesting effects can be observed regarding the different ratios of Fe and Cr ions in the photo-deposition precursor ($0.2 \leq x \leq 0.8$, Figure 3B–F), particularly when comparing with Figure 3A,G which correspond to using single metal ions, $\text{Cr}_0\text{Fe}_1\text{-WT}$ and $\text{Cr}_1\text{Fe}_0\text{-WT}$, respectively. Remarkably, with the introduction of a low ratio of Cr ions in the photo-deposition precursor, in the case of $\text{Cr}_{0.2}\text{Fe}_{0.8}\text{-WT}$ and $\text{Cr}_{0.4}\text{Fe}_{0.6}\text{-WT}$, smaller rounded nanoparticles (diameter ≤ 25 nm) were deposited onto the edge of the WT nanotubes (Figure 3B,C). However, with a more increasing Cr ratio, e.g., $\text{Cr}_{0.5}\text{Fe}_{0.5}\text{-WT}$, a well-decorated amorphous composite of Cr and Fe as a uniform film on the top of WT was observed (Figure 3D). In the case of $\text{Cr}_{0.6}\text{Fe}_{0.4}\text{-WT}$, a similar coated film is noticeable with an agglomeration of nanoparticles on the top of the film (Figure 3E). In the case of $\text{Cr}_{0.8}\text{Fe}_{0.2}\text{-WT}$, there is no trace of the above-mentioned film covering the WT surface. Nanoparticles are homogeneously deposited on the WT surface and few partial agglomerations are ob-

served on the WT surface (Figure 3F). It can be stated that the Fe photo-deposition rate is higher than that of Cr (comparing Figure 3A,G) since, in the case of $\text{Cr}_1\text{Fe}_0\text{-WT}$, fewer and smaller nanoparticles can be seen all over the edge of open-top WT nanotubes.

The elemental EDS and EDS-mapping images were provided in Figure 4A–C and Figures S1 and S2 (Supplementary Materials), revealing the presence of Ti and O elements, as well as W, Fe, and Cr which confirmed the successfully fabricated $\text{Cr}_x\text{Fe}_{1-x}\text{-WT}$ photoelectrodes. It can be clearly seen that the Fe and Cr were homogeneously distributed on the surface of WT, as demonstrated by the elemental mapping (Figures S1 and S2 (Supplementary Materials)). The amount of Fe and Cr deposited on the surface of WT, listed in Table S1, showed that Fe has a rather higher photo-deposition rate than that of Cr; comparing the $\text{Cr}_0\text{Fe}_1\text{-WT}$ and $\text{Cr}_1\text{Fe}_0\text{-WT}$. This result can explain the SEM results where bigger and more agglomerations of Fe particles were obtained rather than that of Cr (Figure 3A,G).

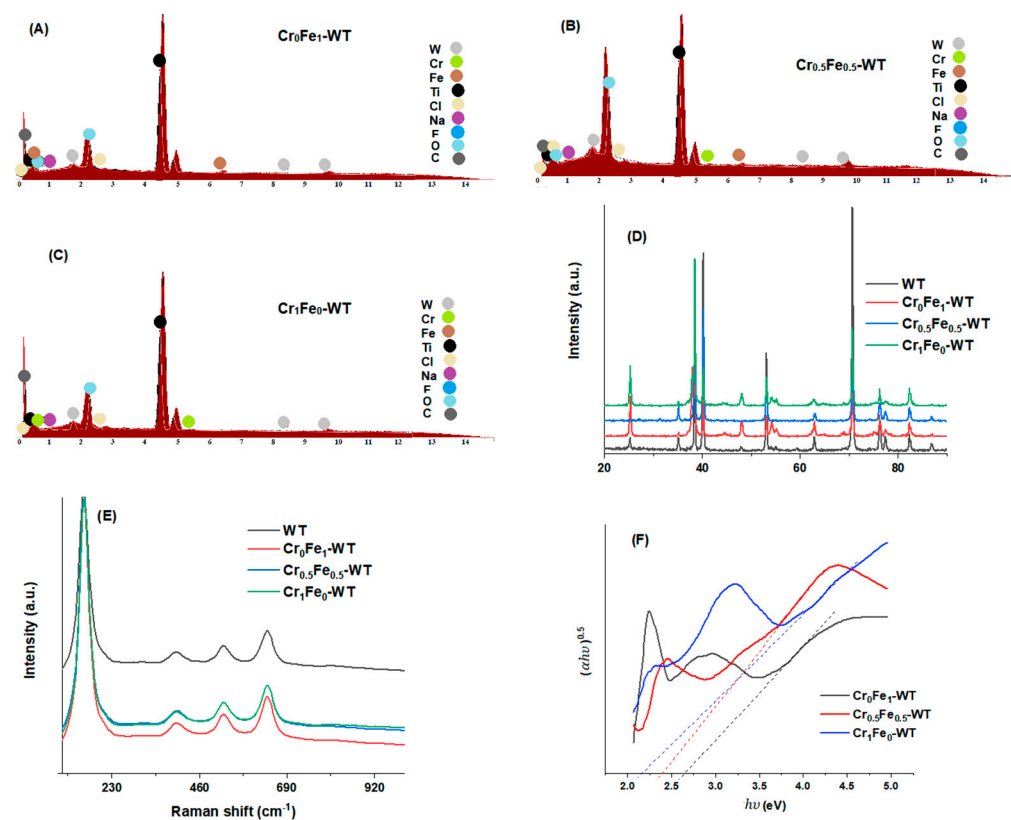


Figure 4. EDX (A–C), XRD (D), Raman (E), and Tauc plot (F) of $\text{Cr}_x\text{Fe}_{1-x}\text{-WT}$ ($x = 0, 0.5, \text{ and } 1$).

The X-ray diffractograms of TiO_2 NTs, WT, $\text{Cr}_0\text{Fe}_1\text{-WT}$, $\text{Cr}_{0.5}\text{Fe}_{0.5}\text{-WT}$, and $\text{Cr}_1\text{Fe}_0\text{-WT}$ are shown in Figure 4D. Generally, similar XRD patterns were observed for all measured photoelectrodes but $\text{Cr}_{0.5}\text{Fe}_{0.5}\text{-WT}$. Diffraction peaks can be assigned to metallic Ti substrate and TiO_2 at its anatase phase with evidence of the peaks at 2θ of 25.3° , 37.8° , 48.1° , 53.9° , and 70.3° which could be attributed to the (101), (004), (200), (105), and (220) planes of anatase, respectively (ICDD-JCPD: 01-086-1156). The crystalline phase of tungsten (W) was not detected by XRD in the samples which can be due to the incorporation of a low concentration of W^{+6} and Ti^{+4} are so close to each other as explained in our previous reports [13,31]. In the case of $\text{Fe}_{0.5}\text{Cr}_{0.5}\text{-WT}$ as shown in the XRD pattern, the anatase peaks at 25.3° and 48.1° were not detected. That can be attributed to deposited amorphous $\text{Cr}_{0.5}\text{Fe}_{0.5}$ film which covered the top of the WT photoelectrode as mentioned in SEM results (Figure 3D). There is no sign of Fe or Cr crystalline phase in XRD patterns. However, this result does not exclude the possible deposited amorphous phase of $\text{Cr}_x\text{Fe}_{1-x}$ at the surface of WT.

Raman was employed to further structural analysis of $\text{Cr}_x\text{Fe}_{1-x}$ -WT photoelectrodes. The characteristic peaks observed at 159, 401, 520, and 637 cm^{-1} are consistent with those of anatase TiO_2 ; corresponding to Eg, B1g, A1g, and Eg, respectively (Figure 4E). No crystalline phases related to other species were observed.

The optical properties of $\text{Cr}_x\text{Fe}_{1-x}$ -WT photoelectrodes were also studied (Figure S3 (Supplementary Materials)) and the band gaps of photoelectrodes have been estimated from the Tauc plot (Figures 4F and S3). $\text{Cr}_x\text{Fe}_{1-x}$ -WT ($0 \leq x \leq 1$) photoelectrodes exhibit better visible region absorption than that of pristine WT, especially in the case of using Cr ions for the WT surface modification. The estimated band gaps were found to be in the range of 2.16–2.65 eV after the photo-deposition of $\text{Cr}_x\text{Fe}_{1-x}$, ($0 \leq x \leq 1$) on the WT surface (Table S2). As can be seen in Figure S3, in the case of Cr_1Fe_0 -WT, a peak around 550 nm was observed that belongs to the presence of Cr on the surface of WT photoelectrodes. This kind of peak, $\lambda > 500\text{ nm}$, was also observed in other literature [26,32].

3.2. PEC Characterization

LSV measurements were performed to examine the photo-sensitivity of $\text{Cr}_x\text{Fe}_{1-x}$ -WT by recording current density as responses of as-prepared photoelectrodes, through scanning the voltage in the dark, under illumination, and by switching the light on and off (Figures 5A,B and S4). The current density of $\text{Cr}_x\text{Fe}_{1-x}$ -WT is near zero in the dark (Figure 5A) and significant light sensitivity was observed under light illumination for all $\text{Cr}_x\text{Fe}_{1-x}$ -WT photoelectrodes. In some cases, particularly $\text{Cr}_{0.5}\text{Fe}_{0.5}$ -WT, an anodic peak centered at +0.75 V was observed which can be assigned to surface oxidation of the deposited amorphous composite $\text{Cr}_x\text{Fe}_{1-x}$ ($0.5 \leq x \leq 0.6$) film on the surface of WT photoelectrode (see Figure 3D,E). $\text{Cr}_{0.8}\text{Fe}_{0.2}$ -WT showed the maximum photocurrent density. It achieved a value of 0.48 mA cm^{-2} at 1.23 V vs. RHE, which corresponds to a ~2 times increase compared to the pristine WT (Figure 5B). The chopped light polarization curves revealed that $\text{Cr}_x\text{Fe}_{1-x}$ -WT ($0 \leq x \leq 1$) photoelectrodes have good repeatability and stability during light irradiation (Figure S5).

Chronoamperometry (CA) measurement was conducted to evaluate the stability of the photocurrent density of $\text{Cr}_x\text{Fe}_{1-x}$ -WT (Figure 5C). The response of $\text{Cr}_x\text{Fe}_{1-x}$ -WT photoelectrodes to light is rapid and after the initial spike, the photocurrent decreases due to the strong e^-/h^+ recombination and then stabilizes less than 60 s. Generally, the current density of pristine WT was increased after the surface modification. The photocurrent density of pristine WT was 0.43 mA cm^{-2} which enhanced to 0.63 mA cm^{-2} for the $\text{Cr}_{0.8}\text{Fe}_{0.2}$ -WT photoelectrode at a bias of +1.62 V vs. RHE (Figure 5C). Highly sensitive photocurrent responses were observed upon switching the light on and off. The photocurrent was enhanced significantly under illumination and returned to near zero value as the light was turned off (Figure 5D).

Open circuit potential (OCP) of pristine WT and $\text{Cr}_x\text{Fe}_{1-x}$ -WT photoelectrodes were investigated to study photovoltage as well as the lifetime of photo-generated e^-/h^+ . Characteristic behavior of an n-type semiconducting material was observed (Figure 6A); upon illumination, the potential of $\text{Cr}_x\text{Fe}_{1-x}$ -WT shifts to more negative values. Afterward, when the light is turned off, the potential of $\text{Cr}_x\text{Fe}_{1-x}$ -WT increases back to near initial values prior to the illumination and a decay profile appears. In all $\text{Cr}_x\text{Fe}_{1-x}$ -WT photoelectrodes, a fast change in OCP was observed after the light is switched on which correlated with the fast response to light in photocurrent measurements. The photovoltages are $\geq 400\text{ mV}$, which suggests a significant concentration of photo-generated electrons (Figure 6A). The higher photovoltages for $\text{Cr}_x\text{Fe}_{1-x}$ -WT were obtained rather than that of pristine WT, suggesting a more remarkable photo response after the WT surface modification. Moreover, it has been reported that the decay profile of OCP after turning the light off represents the charge recombination kinetics (Figure 6B) [9,13].

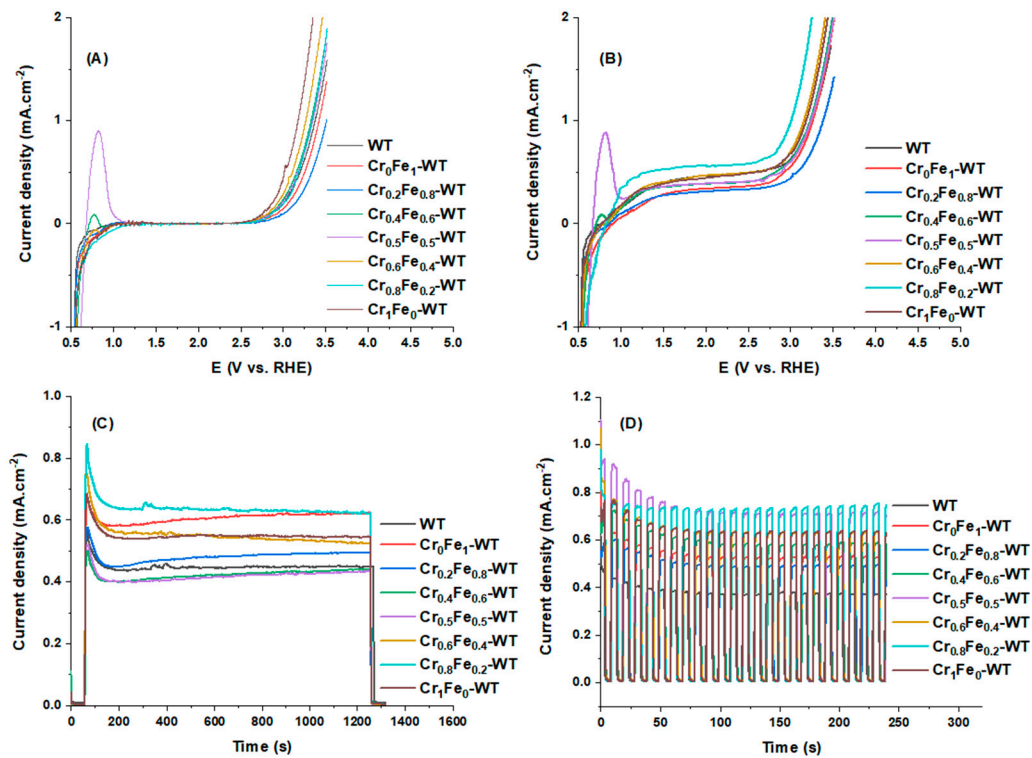


Figure 5. LSV of $\text{Cr}_x\text{Fe}_{1-x}\text{-WT}$ in the dark (A), and under light illumination (B), photocurrent response curves at a given +1.62 V vs. RHE (C) and chopped light (D) in KOH (1 M, pH = 13.9) solution containing ethylene glycol (5 vol%).

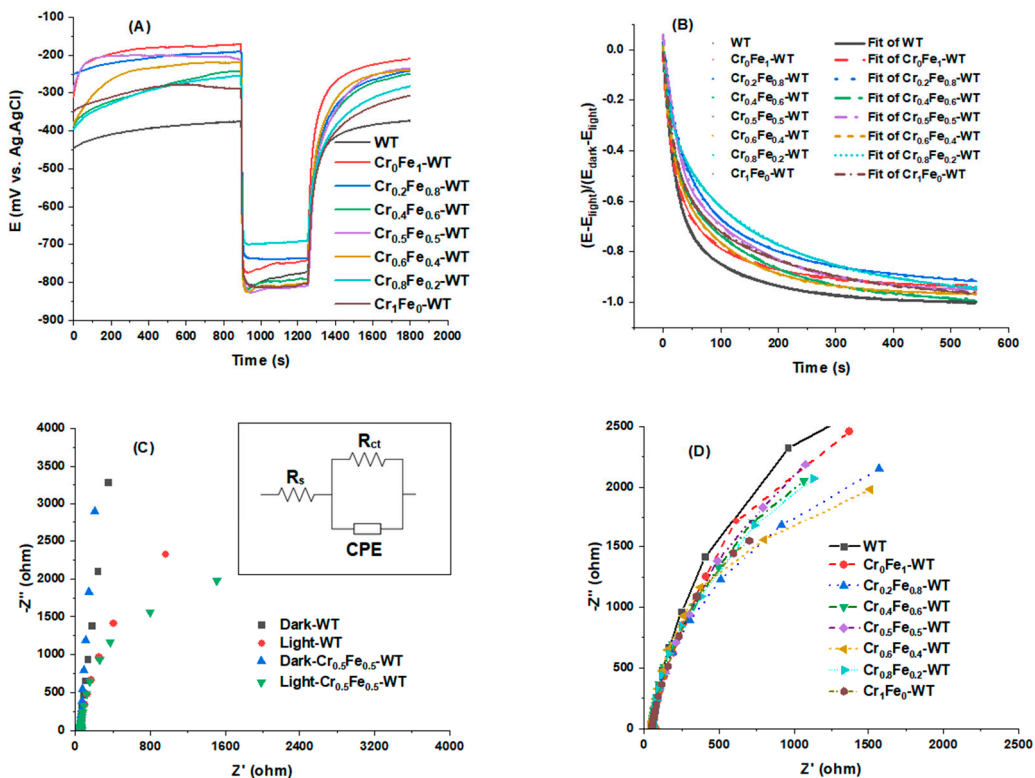


Figure 6. OCP (A) and fitted decay profile of $\text{Cr}_x\text{Fe}_{1-x}\text{-WT}$ (B), EIS plots in the dark and light (inset: equivalent circuit model used for fitting EIS data) (C), and EIS plots under light illumination for all photoelectrodes at a bias of 1.22 V vs. RHE (D).

Then, by fitting OCP decay profiles with a bi-exponential function (Equation (2)), the average recombination lifetime of photo charges was calculated.

$$V(t) = V_0 + A_1 e^{-\frac{t}{\tau_1}} + A_2 e^{-\frac{t}{\tau_2}} \quad (2)$$

where V , t , V_0 , A_1 and A_2 are potential decay, time, fitting constants, and τ_1 and τ_2 are exponential lifetime components for recombination processes in the bulk and surface, respectively.

The harmonic mean of decay lifetime (τ_m) is calculated by Equation (3) and the data are summarized in Table S3.

$$\tau_m = (A_1 \tau_1 \times A_2 \tau_2) / (A_1 A_2) \quad (3)$$

The longest photo charge lifetime was obtained in the case of $\text{Cr}_{0.8}\text{Fe}_{0.2}$ -WT photoelectrode, indicating more efficient charge recombination suppression compared with other $\text{Cr}_x\text{Fe}_{1-x}$ -WT photoelectrodes.

To further confirm the e^-/h^+ separation and transfer of photogenerated carriers, electrochemical impedance spectroscopy (EIS) was measured. EIS data under the dark and light illumination have been plotted as Nyquist plots in Figure 6C,D, fitted by the equivalent circuit model (the inset plot in Figure 6C) to simulate the Nyquist plots. R_s is the uncompensated solution resistance, R_{ct} denotes the charge transfer resistance, and CPE is defined as CPE-T and CPE-P, representing the constant phase elements. The fitting impedance parameter values are listed in Table 1.

Table 1. EIS fitting parameters of $\text{Cr}_x\text{Fe}_{1-x}$ -WT photoelectrodes under illumination.

Photoelectrode	R_{ct} ($\text{k}\Omega\text{cm}^{-2}$)	CPE		
		n	Q (μFcm^{-2})	C (μFcm^{-2})
WT	7.247	0.97	71.9	70.3
Cr_0Fe_1 -WT	7.541	0.90	106	104
$\text{Cr}_{0.2}\text{Fe}_{0.8}$ -WT	9.670	0.92	86.0	84.7
$\text{Cr}_{0.4}\text{Fe}_{0.6}$ -WT	5.716	0.95	73.8	70.4
$\text{Cr}_{0.5}\text{Fe}_{0.5}$ -WT	6.511	0.94	81.3	78.3
$\text{Cr}_{0.6}\text{Fe}_{0.4}$ -WT	4.253	0.95	81.9	77.8
$\text{Cr}_{0.8}\text{Fe}_{0.2}$ -WT	3.420	0.94	88.3	81.8
Cr_1Fe_0 -WT	10.016	0.91	117	119

The diameter of the semicircle of the Nyquist plot represents the photoelectrode charge transfer resistance and the smaller arc radius means better e^-/h^+ separation efficiency (Figure 6C,D). The charge transfer resistances of photoelectrodes under light illumination are much smaller than those obtained in the dark (Figure 6C). Moreover, the $\text{Cr}_{0.8}\text{Fe}_{0.2}$ -WT photoelectrode showed the smallest R_{ct} value, indicating better charge separation and faster charge transfer kinetics at the electrode interface.

3.3. PEC Water Splitting and H_2 Generation

PEC water splitting using $\text{Cr}_x\text{Fe}_{1-x}$ -WT photoelectrodes was conducted via an inverted burette setup (Figure 1C). The volume of H_2 production was then quantitatively recorded according to the variation of the electrolyte level in the burette every 5 min. As can be seen (Figure 7A), the $\text{Cr}_{0.8}\text{Fe}_{0.2}$ -WT photoelectrode produced more H_2 than that of pristine WT and other photoelectrodes in an alkaline electrolyte. Water splitting for H_2 evolution using $\text{Cr}_{0.8}\text{Fe}_{0.2}$ -WT conducted during four cycles of 60 min (Figure 7B) showed no significant decrease in activity during consecutive cycles, which proves the good stability of the as-prepared electrodes in the PEC water splitting. The PEC evolved H_2 in this work compared with some of the other materials used in PEC water splitting in Table 2.

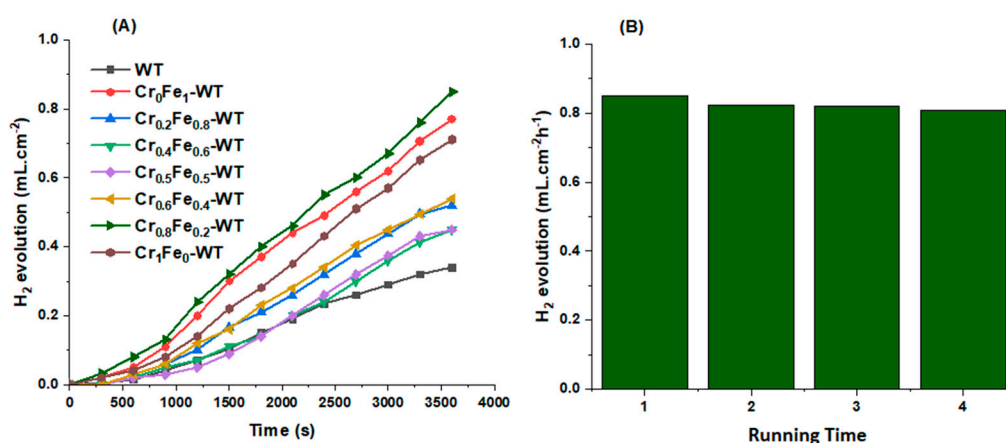


Figure 7. PEC H₂ evolution of Cr_xFe_{1-x}-WT during 1 h at 1.5 V vs. RHE (A), reusability examination of the Cr_{0.8}Fe_{0.2}-WT photoelectrode (B) in KOH (1 M, pH = 13.9) solution containing ethylene glycol (5 vol%).

Table 2. Comparison of H₂ evolution using TiO₂-based nanomaterials.

Photoelectrode	Electrolyte	Light Source	Rate of H ₂ Evolution	Ref.
TiO ₂ NP	MeOH + H ₂ O	150 W halide	0.270 μmol g ⁻¹ min ⁻¹	[33]
1Pt-3WO ₃ -TiO ₂ NTs	H ₂ O +20 vol% EtOH	UV	5 μL h ⁻¹	[34]
Cr-doped TiO ₂ NTs	NaOH	Vis	9.70 μL cm ⁻² h ⁻¹	[35]
Pd-TiO ₂ NTs	H ₂ O +50 vol% MeOH	UV	70 μL cm ⁻² h ⁻¹	[36]
Ru-TiO ₂ NTs	Na ₂ SO ₄ (2 M)	Vis	29 μmol cm ⁻² h ⁻¹	[37]
Fe-TiO ₂ NTs	NaOH	Vis	10 μL cm ⁻² h ⁻¹	[38]
Cu-TiO ₂	H ₂ O +50 vol% EtOH	UV	81.1 μmol g ⁻¹ h ⁻¹	[20]
Cr _{0.8} Fe _{0.2} -WT	KOH + 10 vol% EG	Vis	0.85 mL cm ⁻² h ⁻¹	This work

4. Conclusions

A simple and effective surface modification was applied by photo-deposition of a single ion of Fe, Cr, as well as dual ions (Cr_xFe_{1-x}, 0 ≤ x ≤ 1) on the surface of WT to fabricate Cr_xFe_{1-x}-WT photoelectrodes. The determined band gaps of the photoelectrodes using Tauc plots were in a range of 2.16–2.65 eV which is less than pristine WT. The ratio of Fe and Cr showed a significant effect on the deposition rate. In some ratios, an amorphous layer of Cr_xFe_{1-x} (0.5 ≤ x ≤ 0.6) covered the WT surface which is unfavorable for the separation of photo-generated e⁻/h⁺ and consequently decreases the PEC efficiency of these photoelectrodes. The Cr and Fe doping individually might improve the photocurrent by expended visible light absorbance as well as the effective separation of photo-generated e⁻/h⁺. However, the ratio of dual co-catalysts should be carefully optimized. On the other hand, Cr_{0.8}Fe_{0.2}-WT made a great improvement in PEC activities. Better PEC activity of Cr_{0.8}Fe_{0.2}-WT can be due to less charge transfer resistance as well as a longer photo charge lifetime. The maximum evolved H₂ was also obtained for Cr_{0.8}Fe_{0.2}-WT photoelectrodes which are over two times that of pristine WT.

Supplementary Materials: The following supporting information can be downloaded at: <https://www.mdpi.com/article/10.3390/su142013251/su142013251/s1>, Figure S1: EDS mapping of Cr₀Fe₁-WT, Figure S2: EDS mapping of Cr₁Fe₀-WT; Figure S3: UV-Vis spectra (inset: Tauc plot) of Cr_xFe_{1-x}-WT; Figure S4: LSV of Cr_xFe_{1-x}-WT under chopped light; Table S1: The elements ratio obtained by EDS in Cr_xFe_{1-x}-WT; Table S2: The estimated band gap (BG) of Cr_xFe_{1-x}-WT; Table S3: Parameters obtained from OCP decay profiles according to a dual exponentials decay of Cr_xFe_{1-x}-WT.

Author Contributions: Conceptualization, T.M., Y.G., T.S., and M.M.M.; formal analysis, T.M., S.S. and T.S.; investigation, T.M. and S.S.; data curation, T.M. and Y.G.; writing—original draft preparation, T.M.; writing—review and editing, T.S. and S.S.; supervision, Y.G. and M.M.M.; funding acquisition, Y.G. All authors have read and agreed to the published version of the manuscript.

Funding: This work was supported by the Isfahan University of Technology.

Institutional Review Board Statement: Not applicable.

Informed Consent Statement: Not applicable.

Data Availability Statement: The data presented in this study are available on request from the corresponding author.

Acknowledgments: The financial support of the Research Council of the Isfahan University of Technology is gratefully acknowledged.

Conflicts of Interest: The authors declare no conflict of interest.

References

1. Nazir, H.; Muthuswamy, N.; Louis, C.; Jose, S.; Prakash, J.; Buan, M.E.; Flox, C.; Chavan, S.; Shi, X.; Kauranen, P. Is the H₂ economy realizable in the foreseeable future? Part III: H₂ usage technologies, applications, and challenges and opportunities. *Int. J. Hydrogen Energy* **2020**, *45*, 28217–28239. [[CrossRef](#)] [[PubMed](#)]
2. Wang, M.; Wang, G.; Sun, Z.; Zhang, Y.; Xu, D. Review of renewable energy-based hydrogen production processes for sustainable energy innovation. *Glob. Energy Interconnect.* **2019**, *2*, 436–443. [[CrossRef](#)]
3. Fujishima, A.; Honda, K. Electrochemical Photolysis of Water at a Semiconductor Electrode. *Nature* **1972**, *238*, 37–38. [[CrossRef](#)]
4. Kalanur, S.S.; Duy, L.T.; Seo, H. Recent Progress in Photoelectrochemical Water Splitting Activity of WO₃ Photoanodes. *Top. Catal.* **2018**, *61*, 1043–1076. [[CrossRef](#)]
5. Sivula, K.; Le Formal, F.; Grätzel, M. Solar Water Splitting: Progress Using Hematite (α -Fe₂O₃) Photoelectrodes. *ChemSusChem* **2011**, *4*, 432–449. [[CrossRef](#)]
6. dos Santos, W.S.; Rodriguez, M.; Khoury, J.M.O.; Nascimento, L.A.; Ribeiro, R.J.P.; Mesquita, J.P.; Silva, A.C.; Nogueira, F.G.E.; Pereira, M.C. Bismuth Vanadate Photoelectrodes with High Photovoltage as Photoanode and Photocathode in Photoelectrochemical Cells for Water Splitting. *ChemSusChem* **2018**, *11*, 589–597. [[CrossRef](#)] [[PubMed](#)]
7. Liu, J.; Li, S.; Dewil, R.; Vanierschot, M.; Baeyens, J.; Deng, Y. Water Splitting by MnO_x/Na₂CO₃ Reversible Redox Reactions. *Sustainability* **2022**, *14*, 7597. [[CrossRef](#)]
8. Yu, Z.; Liu, H.; Zhu, M.; Li, Y.; Li, W. Interfacial Charge Transport in 1D TiO₂ Based Photoelectrodes for Photoelectrochemical Water Splitting. *Small* **2021**, *17*, 1903378. [[CrossRef](#)] [[PubMed](#)]
9. Sharifi, T.; Ghayeb, Y.; Mohammadi, T.; Momeni, M.M.; Bagheri, R.; Song, Z. Surface treatment of titanium by in-situ anodization and NiO photodeposition: Enhancement of photoelectrochemical properties for water splitting and photocathodic protection of stainless steel. *Appl. Phys. A* **2021**, *127*, 72. [[CrossRef](#)]
10. Zhao, Y.; Hoivik, N.; Wang, K. Recent advance on engineering titanium dioxide nanotubes for photochemical and photoelectrochemical water splitting. *Nano Energy* **2016**, *30*, 728–744. [[CrossRef](#)]
11. Ge, M.; Li, Q.; Cao, C.; Huang, J.; Li, S.; Zhang, S.; Chen, Z.; Zhang, K.; Al-Deyab, S.S.; Lai, Y. One-dimensional TiO₂ nanotube photocatalysts for solar water splitting. *Adv. Sci.* **2017**, *4*, 1600152. [[CrossRef](#)]
12. Natarajan, T.S.; Natarajan, K.; Bajaj, H.C.; Tayade, R.J. Enhanced photocatalytic activity of bismuth-doped TiO₂ nanotubes under direct sunlight irradiation for degradation of Rhodamine B dye. *J. Nanoparticle Res.* **2013**, *15*, 1669. [[CrossRef](#)]
13. Mohammadi, T.; Ghayeb, Y.; Sharifi, T.; Momeni, M.M. RuO₂ photodeposited on W-doped and Cr-doped TiO₂ nanotubes with enhanced photoelectrochemical water splitting and capacitor properties. *New J. Chem.* **2020**, *44*, 2339–2349. [[CrossRef](#)]
14. Huo, K.; Gao, B.; Fu, J.; Zhao, L.; Chu, P.K. Fabrication, modification, and biomedical applications of anodized TiO₂ nanotube arrays. *Rsc Adv.* **2014**, *4*, 17300–17324. [[CrossRef](#)]
15. Sharifi, T.; Mohammadi, T.; Momeni, M.M.; Kusic, H.; Kraljic Rokovic, M.; Loncaric Bozic, A.; Ghayeb, Y. Influence of Photo-Deposited Pt and Pd onto Chromium Doped TiO₂ Nanotubes in Photo-Electrochemical Water Splitting for Hydrogen Generation. *Catalysts* **2021**, *11*, 212. [[CrossRef](#)]
16. Tobaldi, D.M.; Kočí, K.; Edelmannová, M.; Lajaunie, L.; Figueiredo, B.; Calvino, J.J.; Seabra, M.P.; Labrincha, J.A. Cu_xO and carbon-modified TiO₂-based hybrid materials for photocatalytically assisted H₂ generation. *Mater. Today Energy* **2021**, *19*, 100607. [[CrossRef](#)]
17. Huerta-Flores, A.M.; Chávez-Angulo, G.; Carrasco-Jaim, O.A.; Torres-Martínez, L.M.; Garza-Navarro, M.A. Enhanced photoelectrochemical water splitting on heterostructured α -Fe₂O₃-TiO₂:X (X = Co, Cu, Bi) photoanodes: Role of metal doping on charge carrier dynamics improvement. *J. Photochem. Photobiol. A Chem.* **2021**, *410*, 113077. [[CrossRef](#)]
18. Draz, M.A.; El-Maghrabi, H.H.; Soliman, F.S.; Selim, H.; Razik, A.A.; Amin, A.E.-s.; Moustafa, Y.M.; Hamdy, A.; Nada, A.A. Large scale hybrid magnetic ZnFe₂O₄/TiO₂ nanocomposite with highly photocatalytic activity for water splitting. *J. Nanopart. Res.* **2021**, *23*, 10. [[CrossRef](#)]
19. Liang, Z.; Chen, D.; Xu, S.; Fang, Z.; Wang, L.; Yang, W.; Hou, H. Synergistic promotion of photoelectrochemical water splitting efficiency of TiO₂ nanorod arrays by doping and surface modification. *J. Mater. Chem. C* **2021**, *9*, 12263–12272. [[CrossRef](#)]
20. Montoya, A.T.; Gillan, E.G. Enhanced Photocatalytic Hydrogen Evolution from Transition-Metal Surface-Modified TiO₂. *ACS Omega* **2018**, *3*, 2947–2955. [[CrossRef](#)]

21. Šuligoj, A.; Arčon, I.; Mazaj, M.; Dražić, G.; Arčon, D.; Cool, P.; Štangar, U.L.; Tušar, N.N. Surface modified titanium dioxide using transition metals: Nickel as a winning transition metal for solar light photocatalysis. *J. Mater. Chem. A* **2018**, *6*, 9882–9892. [[CrossRef](#)]
22. Wenderich, K.; Mul, G. Methods, Mechanism, and Applications of Photodeposition in Photocatalysis: A Review. *Chem. Rev.* **2016**, *116*, 14587–14619. [[CrossRef](#)] [[PubMed](#)]
23. Tada, H.; Jin, Q.; Iwaszuk, A.; Nolan, M. Molecular-scale transition metal oxide nanocluster surface-modified titanium dioxide as solar-activated environmental catalysts. *J. Phys. Chem. C* **2014**, *118*, 12077–12086. [[CrossRef](#)]
24. Shopova-Gospodinova, D.; Jeurgens, L.P.; Welzel, U.; Bauermann, L.P.; Hoffmann, R.C.; Bill, J. Synthesis of V-doped TiO₂ films by chemical bath deposition and the effect of post-annealing on their properties. *Thin Solid Films* **2012**, *520*, 5928–5935. [[CrossRef](#)]
25. Kyeremateng, N.A.; Lebouin, C.; Knauth, P.; Djenizian, T. The electrochemical behaviour of TiO₂ nanotubes with Co₃O₄ or NiO submicron particles: Composite anode materials for Li-ion micro batteries. *Electrochim. Acta* **2013**, *88*, 814–820. [[CrossRef](#)]
26. Sharifi, T.; Ghayeb, Y.; Mohammadi, T.; Momeni, M.M. Enhanced photoelectrochemical water splitting of CrTiO₂ nanotube photoanodes by the decoration of their surface via the photodeposition of Ag and Au. *Dalton Trans.* **2018**, *47*, 11593–11604. [[CrossRef](#)]
27. Hariri, A.; Gilani, N.; Pasikhani, J.V. Promoting the photo-induced charge separation and photoelectrocatalytic hydrogen generation: Z-scheme configuration of WO₃ quantum nanodots-decorated immobilized Ti/TiO₂ nanorods. *J. Alloys Compd.* **2021**, *871*, 159528. [[CrossRef](#)]
28. Yang, B.; Chai, Y.; Yang, F.; Zhang, Q.; Liu, H.; Wang, N. Hydrogen generation by aluminum-water reaction in acidic and alkaline media and its reaction dynamics. *Int. J. Energy Res.* **2018**, *42*, 1594–1602. [[CrossRef](#)]
29. Mishra, P.; Shukla, P.; Srivastava, O. Study of modular PEC solar cells for photoelectrochemical splitting of water employing nanostructured TiO₂ photoelectrodes. *Int. J. Hydrogen Energy* **2007**, *32*, 1680–1685. [[CrossRef](#)]
30. Momeni, M.M.; Ghayeb, Y.; Davarzadeh, M. Single-step electrochemical anodization for synthesis of hierarchical WO₃-TiO₂ nanotube arrays on titanium foil as a good photoanode for water splitting with visible light. *J. Electroanal. Chem.* **2015**, *739*, 149–155. [[CrossRef](#)]
31. Momeni, M.M.; Akbarnia, M.; Ghayeb, Y. Preparation of S-W-codoped TiO₂ nanotubes and effect of various hole scavengers on their photoelectrochemical activity: Alcohol series. *Int. J. Hydrogen Energy* **2020**, *45*, 33552–33562. [[CrossRef](#)]
32. Yang, Y.; Wang, G.; Gu, G.; Li, Q.; Kang, S.; Zhang, Y.; Ng, D.H.; Zhao, H. One pot microwave-assisted synthesis of Ag decorated yolk@ shell structured TiO₂ microspheres. *Rsc Adv.* **2015**, *5*, 11349–11357. [[CrossRef](#)]
33. D’Elia, D.; Beauger, C.; Hochepped, J.-F.; Rigacci, A.; Berger, M.-H.; Keller, N.; Keller-Spitzer, V.; Suzuki, Y.; Valmalette, J.-C.; Benabdesselam, M.; et al. Impact of three different TiO₂ morphologies on hydrogen evolution by methanol assisted water splitting: Nanoparticles, nanotubes and aerogels. *Int. J. Hydrogen Energy* **2011**, *36*, 14360–14373. [[CrossRef](#)]
34. Spanu, D.; Recchia, S.; Mohajernia, S.; Schmuki, P.; Altomare, M. Site-selective Pt dewetting on WO₃-coated TiO₂ nanotube arrays: An electron transfer cascade-based H₂ evolution photocatalyst. *Appl. Catal. B Environ.* **2018**, *237*, 198–205. [[CrossRef](#)]
35. Momeni, M.M.; Ghayeb, Y. Photoelectrochemical water splitting on chromium-doped titanium dioxide nanotube photoanodes prepared by single-step anodizing. *J. Alloys Compd.* **2015**, *637*, 393–400. [[CrossRef](#)]
36. Nguyen, N.T.; Ozkan, S.; Hejazi, S.; Denisov, N.; Tomanec, O.; Zboril, R.; Schmuki, P. Providing significantly enhanced photocatalytic H₂ generation using porous PtPdAg alloy nanoparticles on spaced TiO₂ nanotubes. *Int. J. Hydrogen Energy* **2019**, *44*, 22962–22971. [[CrossRef](#)]
37. Li, F.; Huang, H.; Li, G.; Leung, D.Y. TiO₂ nanotube arrays modified with nanoparticles of platinum group metals (Pt, Pd, Ru): Enhancement on photoelectrochemical performance. *J. Nanopart. Res.* **2019**, *21*, 29. [[CrossRef](#)]
38. Momeni, M.M.; Ghayeb, Y. Fabrication, characterization and photoelectrochemical behavior of Fe-TiO₂ nanotubes composite photoanodes for solar water splitting. *J. Electroanal. Chem.* **2015**, *751*, 43–48. [[CrossRef](#)]